

Ab Initio Many Body Quantum Embedding and Local Correlation in Crystalline Materials using Interpolative Separable Density Fitting

Junjie Yang,^{1, 2} Ning Zhang,^{1, 3} Shunyue Yuan,^{2, 4} Jincheng Yu,⁵ Hong-Zhou Ye,^{5, 6} and Garnet Chan^{1, 2, *}

¹*Division of Chemistry and Chemical Engineering,*

California Institute of Technology, Pasadena, California 91125, USA

²*Marcus Center for Theoretical Chemistry, California Institute of Technology, Pasadena, California 91125, USA*

³*Qingdao Institute for Theoretical and Computational Sciences and Center for Optics Research and Engineering, Shandong University, Qingdao, Shandong 266237, China*

⁴*Division of Engineering and Applied Sciences, California Institute of Technology, Pasadena, California 91125, USA*

⁵*Department of Chemistry and Biochemistry, University of Maryland, College Park, Maryland, 20742, USA*

⁶*Institute for Physical Science and Technology, University of Maryland, College Park, Maryland, 20742, USA*

We present an efficient implementation of ab initio many-body quantum embedding and local correlation methods for infinite periodic systems through translational symmetry adapted interpolative separable density fitting, an approach which reduces the scaling of the calculations to only linear with the number of k-points. Employing this methodology, we compute correlated ground-state coupled cluster energies within density matrix embedding and local natural orbital correlation frameworks for both weakly and strongly correlated solids, using up to 1000 k-points. By extrapolating the local correlation domains and k-point sampling we further obtain estimates of the full coupled cluster with singles, doubles, and perturbative triples ground-state energies in the thermodynamic limit.

I. INTRODUCTION

Correlated wavefunction methods have attracted increasing attention in computational materials science, because they provide a pathway to controllable accuracy via systematically improvable many-body expansions [1–11]. However, despite their theoretical advantages, these approaches naively suffer from steep computational scaling with system size, which presents an obstacle to obtaining thermodynamic limit (TDL) results [7, 12–14].

Consequently, several strategies are commonly used to reduce the cost of such calculations. The first exploits the translational symmetry inherent in periodic systems, by utilizing Bloch-type single-particle orbitals labelled by the crystal momentum k . When a uniform k -point mesh of size N_k (containing the Γ point) is employed to sample the Brillouin zone, the calculation is equivalent to one from a periodic supercell containing N_k unit cell images, but with a N_k^{-1} [15] to N_k^{-2} [6] reduction in cost.

The second strategy exploits the locality and decay of correlations [16–18]. This “near-sightedness” is embodied in different quantum embedding and local correlation frameworks. While there are many variations [19–54], a common feature is that the system is divided into multiple fragments (or clusters), with each fragment subsequently treated independently or with a simplified level of coupling, for example, via the self-consistency of a single-particle quantity in quantum embedding methods [54], or through the simplified treatment of weak pairs in certain local correlation methods. In this work, for concreteness we will focus on density matrix embedding [55, 56] as an example of a quantum embedding method, and the local natural orbital (LNO) method [22, 48] as an example of

a local correlation framework. Both have been applied with success to crystalline materials in a diverse range of applications [48, 50–52, 57–60].

The third strategy uses low-rank representations. Low-rank approximations of the Coulomb tensor have been extensively used, such as Cholesky decomposition and resolution-of-the-identity techniques [61–66], pseudospectral approaches [67–69], as well as tensor hypercontraction (THC) [70–73]. Interpolative separable density fitting (ISDF) has attracted attention as a protocol for generating THC-like factorizations in systems under periodic boundary conditions, where it has demonstrated the potential to accelerate multiple electronic structure methods [74–86].

In this work, we describe an implementation of quantum embedding and local correlation for infinite periodic systems that combines the above reduced-scaling strategies. In particular, our methodology exploits translational symmetry through a tensor hypercontraction representation of the Coulomb interaction, implemented via a symmetry adapted ISDF [87–91] based on crystalline orbitals and utilizing the fast Fourier transform (FFTISDF). The primary algorithmic outcome is the ability to perform many-body quantum embedding and local correlation calculations in materials with only linear scaling with the number of k -points. This enables the practical extraction of thermodynamic limit results.

We organize the rest of the work as follows. Section II recalls the FFTISDF algorithm for periodic solids utilizing k -point symmetry, and then describes the efficient implementation of the various components of the density matrix embedding and local natural orbital correlation frameworks in this representation and summarizes the parameters used for the benchmark calculations. Section III provides a set of benchmark studies using coupled cluster theory solvers on representative crystalline systems, including diamond, carbon dioxide, nickel monox-

* gkc1000@gmail.com

ide, and the infinite layer cuprate CaCuO_2 . These calculations employ Gaussian polarized double-zeta basis sets with up to 1000 k-points to demonstrate the method's scalability, and we extract the thermodynamic limit of the coupled cluster energies for several of the systems. Finally, Section IV summarizes our main findings and discusses potential directions for future work.

II. THEORY

Our periodic calculations are performed using a crystalline Gaussian-type orbital(GTO) basis,

$$\phi_{\mu}^{\mathbf{k}}(\mathbf{r}) = \sum_{\mathbf{T}} e^{i\mathbf{k}\cdot\mathbf{T}} \tilde{\phi}_{\mu}(\mathbf{r} - \mathbf{T}) \quad (1)$$

where $\tilde{\phi}_{\mu}(\mathbf{r})$ is a normal GTO centered on an atom in the reference unit cell; \mathbf{T} is a lattice translation vector; and \mathbf{k} is a momentum vector sampled in the first Brillouin zone. Our implementation builds upon the Gaussian-Plane-Wave infrastructure provided by the PySCF package [92–94], where the basis functions are evaluated on a uniform grid in the unit cell at a set of points $\{\mathbf{r}\}$. (This infrastructure is termed FFTDF in PySCF).

A. Periodic k-point FFTISDF representation of integrals

The core idea of the ISDF approach is to approximate products of basis functions on the grid points \mathbf{r} by using values from a select set of interpolating points \mathbf{r}_I (IPs). This reduces the computational complexity of evaluating two-electron integrals while maintaining systematic improbability of the approximation. In this work, the interpolation points are selected using a pivoted Cholesky decomposition of $\phi_{\mu}^{\mathbf{k}}(\mathbf{r})\phi_{\nu}^{\mathbf{k}}(\mathbf{r})^*$ (where \mathbf{r} is the column index) closely following the procedure outlined in Ref. [95]. Only the largest $N_{\text{IP}} = c_{\text{IP}} \times N_{\text{AO}}$ columns are used, where the pre-defined constant c_{IP} controls the accuracy [96]. This method is suitable for systems with moderate unit cell sizes. Although alternative approaches, such as the centroidal Voronoi tessellation k-means algorithm [75], may be more efficient for large unit cells, they are not the focus of this study. The interpolation points are used to approximate the product of basis functions on the uniform grid $\{\mathbf{r}\}$:

$$\begin{aligned} \rho_{\mu\nu}^{\mathbf{k}_{\mu}\mathbf{k}_{\nu}}(\mathbf{r}) &= \phi_{\mu}^{\mathbf{k}_{\mu}}(\mathbf{r}) \phi_{\nu}^{\mathbf{k}_{\nu}}(\mathbf{r})^* = \phi_{\mu}^{\mathbf{k}_{\mu}}(\mathbf{r}) \phi_{\nu}^{-\mathbf{k}_{\nu}}(\mathbf{r}) \\ &\approx \sum_I \xi_I^{\mathbf{q}}(\mathbf{r}) X_{I\mu}^{\mathbf{k}_{\mu}} X_{I\nu}^{-\mathbf{k}_{\nu}} \end{aligned} \quad (2)$$

where in the above equation, $X_{I\mu}^{\mathbf{k}_{\mu}} = \phi_{\mu}^{\mathbf{k}_{\mu}}(\mathbf{r}_I)$ is the interpolating vector (IV); $\mathbf{q} = \mathbf{k}_{\mu} - \mathbf{k}_{\nu} + \mathbf{B}_n$ due to momentum conservation and is shifted to be within the first Brillouin zone (\mathbf{B}_n is an integer multiple of the reciprocal lattice

vectors); and $\xi_I^{\mathbf{q}}(\mathbf{r})$ is the interpolation function. The interpolation function is obtained from solving the least-squares problem corresponding to Eq. 2, which leads to the following linear equation,

$$\mathbf{\Pi}^{\mathbf{q}} \xi^{\mathbf{q}} = \boldsymbol{\eta}^{\mathbf{q}} \quad (3)$$

where $\mathbf{\Pi}^{\mathbf{q}}$ is the metric tensor, defined from the product of IVs,

$$\Pi_{IJ}^{\mathbf{q}} = \sum_{\mathbf{k}} \sum_{\mu\nu} X_{I\mu}^{\mathbf{k}-\mathbf{q}} X_{I\nu}^{-\mathbf{k}} X_{J\mu}^{\mathbf{q}-\mathbf{k}} X_{J\nu}^{\mathbf{k}} \quad (4)$$

and which can be efficiently evaluated using the convolution theorem. Similarly, the right-hand side vector is evaluated as

$$\eta_I^{\mathbf{q}}(\mathbf{r}) = \sum_{\mathbf{k}} \sum_{\mu\nu} X_{I\mu}^{\mathbf{k}-\mathbf{q}} X_{I\nu}^{-\mathbf{k}} \phi_{\mu}^{\mathbf{q}-\mathbf{k}}(\mathbf{r}) \phi_{\nu}^{\mathbf{k}}(\mathbf{r}) \quad (5)$$

The complete algorithm for both the metric tensor and right-hand side vector is outlined in Algorithm 1: when evaluating the metric tensor, $\mathbf{Y}^{\mathbf{k}}$ are IVs, where index f represents IPs and index μ corresponds to the AOs, while for the right-hand side vector, $\mathbf{Y}^{\mathbf{k}}$ represents AO values evaluated on the uniform grid, with index f now labelling the grid points \mathbf{r} .

Algorithm 1 Efficient evaluation of metric tensor and right-hand side vector using convolution theorem.

```

1: Input:  $X_{I\mu}^{\mathbf{k}}$ ,  $Y_{f\mu}^{\mathbf{k}}$ 
2: Output:  $Z_{If}^{\mathbf{q}}$ 
3: for each  $\mathbf{k}$  in the Brillouin zone do
4:    $T_{If}^{\mathbf{k}} = \sum_{\mu} X_{I\mu}^{\mathbf{k}} Y_{f\mu}^{-\mathbf{k}}$ 
5: end for
6:  $T_{If}^{\mathbf{R}} \leftarrow \text{FFT}^{-1}[T_{If}^{\mathbf{k}}]$   $\triangleright$  transform to the supercell space
7:  $Z_{If}^{\mathbf{R}} = T_{If}^{\mathbf{R}} \times T_{If}^{\mathbf{R}}$   $\triangleright$  element-wise multiplication
8:  $Z_{If}^{\mathbf{q}} \leftarrow \text{FFT}[Z_{If}^{\mathbf{R}}]$   $\triangleright$  transform back to the k-space

```

After solving Eq. 3 for the interpolation functions, their Coulomb kernel is defined as

$$W_{IJ}^{\mathbf{q}} = \int d\mathbf{r}_1 d\mathbf{r}_2 \frac{\xi_I^{-\mathbf{q}}(\mathbf{r}_1) \xi_J^{\mathbf{q}}(\mathbf{r}_2)}{|\mathbf{r}_1 - \mathbf{r}_2|} \quad (6)$$

which can be efficiently computed by FFT. Since the interpolation functions are themselves not required and only the Coulomb kernel enters into subsequent calculations, we can in fact determine the Coulomb kernel directly. This can be done by first computing $\mathbf{V}^{\mathbf{q}}$

$$V_{IJ}^{\mathbf{q}} = \int d\mathbf{r}_1 d\mathbf{r}_2 \frac{\eta_I^{-\mathbf{q}}(\mathbf{r}_1) \eta_J^{\mathbf{q}}(\mathbf{r}_2)}{|\mathbf{r}_1 - \mathbf{r}_2|} \quad (7)$$

and then obtaining the Coulomb kernel from solving the

least-squares linear equation,

$$\mathbf{\Pi}^q \mathbf{W}^q \mathbf{\Pi}^q = \mathbf{V}^q \quad (8)$$

Once the ISDF Coulomb kernel is available, the two-electron integrals in the crystalline basis can be expressed in the THC factorized form,

$$(\mu \mathbf{k}_\mu \mathbf{k}_\nu | \lambda \mathbf{k}_\lambda \sigma \mathbf{k}_\sigma) = \sum_{IJ} X_{I\mu}^{\mathbf{k}_\mu} X_{I\nu}^{-\mathbf{k}_\nu} X_{J\lambda}^{\mathbf{k}_\lambda} X_{J\sigma}^{-\mathbf{k}_\sigma} W_{IJ}^q \quad (9)$$

B. Implementation of quantum embedding and local correlation with FFTISDF

Starting from the two-electron integrals in the form of Eq. 9, the various components of quantum embedding and local correlation calculations can be accelerated.

For example, the starting point is typically a periodic Hartree-Fock calculation. The factorized Hamiltonian leads to an efficient evaluation of the exact exchange matrix [87, 88, 91] for the k-point Hartree-Fock (k-HF) theory,

$$\begin{aligned} K_{\mu\nu}^{\mathbf{k}} &= \frac{-1}{N_k} \sum_{IJ} \sum_{\mathbf{q}} X_{I\mu}^{\mathbf{k}} X_{J\nu}^{-\mathbf{k}} W_{IJ}^q \sum_{\lambda\sigma} X_{I\lambda}^{\mathbf{q}-\mathbf{k}} P_{\lambda\sigma}^{\mathbf{k}-\mathbf{q}} X_{J\sigma}^{\mathbf{k}-\mathbf{q}} \\ &= \frac{-1}{N_k} \sum_{IJ} X_{I\mu}^{\mathbf{k}} X_{J\nu}^{-\mathbf{k}} \sum_{\mathbf{q}} W_{IJ}^q \rho_{IJ}^{\mathbf{k}-\mathbf{q}} \end{aligned} \quad (10)$$

which can also be computed as a convolution.

Similarly, in local correlation frameworks it is generally necessary to do a global (i.e. on the whole system) correlation calculation at a low level of theory (e.g. second order perturbation theory or direct random phase approximation), either to determine the virtual correlation space, or to compute a global energy correction [88, 97–100]. The k-point FFTISDF formulation reduces the k-point scaling of such calculations also. In the case of k-point scaled-opposite-spin MP2 (k-SOS-MP2) and the k-point direct random phase approximation (k-dRPA) one can obtain overall linear scaling with the number of k-points [87, 88].

The k-SOS-MP2 correlation energy is defined by multiplying an empirical scaling factor $c_{\text{SOS}} = 1.3$ to the opposite-spin MP2 correlation energy,

$$E_{\text{corr}}^{\text{SOS-MP2}} = c_{\text{SOS}} E_{\text{OS}}, \quad (11)$$

For an efficient formulation, the opposite-spin contribution can be computed via the imaginary-frequency non-interacting density response function [101] (the same expression can be derived from the Laplace-transformed en-

ergy denominator formula [72, 102]),

$$\begin{aligned} E_{\text{OS}} &= \sum_{\mathbf{q}} \int_{-\infty}^{\infty} \frac{d\omega}{2\pi N_k} \text{tr} [\mathbf{P}^q(i\omega) \mathbf{P}^q(i\omega)] \\ &= \sum_{\mathbf{q}} \int_0^{\infty} \frac{d\tau}{N_k} \text{tr} [\mathbf{P}^q(\tau) \mathbf{P}^q(-\tau)] \end{aligned} \quad (12)$$

$\mathbf{P}^q(\tau)$ can be efficiently evaluated with the convolution theorem, using a similar algorithm as in Algorithm 1,

$$P_{IJ}^q(\tau) = \sum_{\mathbf{k}} \sum_K G_{IK}^{\mathbf{k}}(\tau) G_{IK}^{\mathbf{q}-\mathbf{k}}(-\tau) W_{KJ}^q \quad (13)$$

where $G_{IJ}^{\mathbf{k}}(\tau)$ is the imaginary-time non-interacting Green's function in the interpolating point representation,

$$G_{IJ}^{\mathbf{k}}(\tau) = \sum_{\mu\nu} X_{I\mu}^{\mathbf{k}} X_{J\nu}^{-\mathbf{k}} G_{\mu\nu}^{\mathbf{k}}(\tau) \quad (14)$$

and in the atomic orbital basis, the Green's function is given by ($\tau > 0$),

$$\begin{aligned} G_{\mu\nu}^{\mathbf{k}}(+\tau) &= + \sum_{i \in \text{occ}} C_{\mu i}^{\mathbf{k}} C_{i\nu}^{\mathbf{k}} \exp(-\tau \epsilon_i^{\mathbf{k}}) \\ G_{\mu\nu}^{\mathbf{k}}(-\tau) &= - \sum_{a \in \text{vir}} C_{\mu a}^{\mathbf{k}} C_{a\nu}^{\mathbf{k}} \exp(+\tau \epsilon_a^{\mathbf{k}}) \end{aligned} \quad (15)$$

$C_{\mu i}^{\mathbf{k}}$ and $\epsilon_i^{\mathbf{k}}$ ($C_{\mu a}^{\mathbf{k}}$ and $\epsilon_a^{\mathbf{k}}$) are the k-point occupied (virtual) coefficients and energies obtained from a k-HF calculation, respectively.

For the k-dRPA, the correlation energy is

$$E_{\text{corr}}^{\text{dRPA}} = \sum_{\mathbf{q}} \int_{-\infty}^{\infty} \frac{d\omega}{2\pi N_k} \left[\ln \det \mathbf{Q}^q(\omega) + \text{tr} \mathbf{P}^q(\omega) \right] \quad (16)$$

where $\mathbf{Q}^q(\omega) = \mathbf{1} - \mathbf{P}^q(\omega)$, $\mathbf{1}$ is the identity matrix of dimension $N_{\text{IP}} \times N_{\text{IP}}$. Eq. 12 is obtained as the second-order term in the Taylor expansion of the logarithm in Eq. 16. The integrals in Eqs. 12 and 16 can be computed by numerical quadrature. Specifically, in this work we use modified Gauss-Legendre grids on the imaginary axis and Clenshaw-Curtis grids on the real axis.

A common component in both quantum embedding (such as density matrix embedding) and local natural orbital correlation treatments is the need to construct a fragment Hamiltonian in a subset of orbitals of the full problem. We can use the FFTISDF form of the Hamiltonian to accelerate this construction. A similar formulation was previously proposed in Ref. [88]. For a general description of the fragment Hamiltonians in density matrix embedding and local natural orbital correlation frameworks, we refer the reader to Ref. [50] and Ref. [48].

The fragments are defined in terms of a set of fragment

orbitals

$$\phi_p(\mathbf{r}) = \frac{1}{\sqrt{N_k}} \sum_{\mathbf{k}} \sum_{\mu} C_{\mu p}^{\mathbf{k}} \phi_{\mu}^{\mathbf{k}}(\mathbf{r}) \quad (17)$$

where the coefficients $C_{\mu p}^{\mathbf{k}}$ depend on the particulars of the embedding theory or correlation framework. For example, in density matrix embedding, ϕ_p refers to the impurity and bath orbitals, while in local natural orbital correlation, they constitute the occupied and virtual orbitals of the fragment. What is needed is the Hamiltonian expressed in the space spanned by the fragment orbitals $\{\phi_p(\mathbf{r})\}$. The computational bottleneck lies in evaluating the two-body part of this Hamiltonian. One way to obtain the two-body part is to transform from the \mathbf{k} -space crystal orbital Hamiltonian to the fragment space,

$$V_{pqrs} = \frac{1}{N_k^2} \sum_{\mathbf{k}_\mu \mathbf{k}_\nu} \sum_{\mu \nu} \sum_{\mathbf{k}_\lambda \mathbf{k}_\sigma} \sum_{\lambda \sigma} C_{\mu p}^{\mathbf{k}_\mu} C_{\nu q}^{-\mathbf{k}_\nu} C_{\lambda r}^{\mathbf{k}_\lambda} C_{\sigma s}^{-\mathbf{k}_\sigma} \times (\mu \mathbf{k}_\mu \nu \mathbf{k}_\nu | \lambda \mathbf{k}_\lambda \sigma \mathbf{k}_\sigma) \quad (18)$$

By employing the FFTISDF formula from Eq. 9, this transformation can be expressed in the more computationally efficient form:

$$V_{pqrs} = \sum_{\mathbf{q}} \sum_{IJ} R_{I,pq}^{\mathbf{q}} R_{J,rs}^{-\mathbf{q}} W_{IJ}^{\mathbf{q}} \quad (19)$$

where the intermediate tensor is,

$$R_{I,pq}^{\mathbf{q}} = \frac{1}{\sqrt{N_k}} \sum_{\mathbf{k}} \sum_{\mu \nu} X_{I\mu}^{\mathbf{k}} X_{I\nu}^{\mathbf{q}-\mathbf{k}} C_{\mu p}^{\mathbf{k}} C_{\nu q}^{-\mathbf{k}} \quad (20)$$

The convolution theorem can be used to evaluate the intermediate tensor. The procedure is summarized in Algorithm 2. Generating the Hamiltonian with FFTISDF has a cost scaling of $\mathcal{O}(N_k N_{\text{EO}}^2 N_{\text{IP}}^2 + N_k N_{\text{EO}}^4 N_{\text{IP}})$, which is more efficient than the direct evaluation of V_{pqrs} by FFTDF when N_{IP} is much less than the total number of grid points.

Algorithm 2 Pseudocode for computing the two-body part of the embedding Hamiltonian.

```

1: Input:  $X_{I\mu}^{\mathbf{k}}$ ,  $C_{\mu p}^{\mathbf{k}}$ 
2: Output:  $R_{I,pq}^{\mathbf{q}}$ 
3: for all  $\mathbf{k}$  do
4:    $T_{Ip}^{\mathbf{k}} = \sum_{\mu} X_{I\mu}^{\mathbf{k}} C_{\mu p}^{\mathbf{k}}$ 
5: end for
6:  $T_{Ip}^{\mathbf{R}} \leftarrow T_{Ip}^{\mathbf{k}}$                                  $\triangleright$  transform to supercell space
7:  $R_{I,pq}^{\mathbf{R}} = T_{Ip}^{\mathbf{R}} T_{Iq}^{\mathbf{R}}$                  $\triangleright$  outer product
8:  $R_{I,pq}^{\mathbf{k}} \leftarrow R_{I,pq}^{\mathbf{R}}$                    $\triangleright$  transform to k-space

```

C. Parallelization

The \mathbf{k} -point FFTISDF formulation lends itself to parallelization, which we have implemented using MPI. Our approach begins by dividing the real-space grid into optimally sized chunks across available processors, which enables highly efficient parallel evaluation of the right-hand side vector following Eq. 5. We note that this domain decomposition significantly reduces the memory requirements per node while maintaining excellent load balancing across computational resources. The Coulomb kernel $\mathbf{W}^{\mathbf{q}}$ is then computed in parallel for each \mathbf{k} -point using Eqs. 7 and 8. For the numerical integrations required in \mathbf{k} -SOS-MP2 and \mathbf{k} -RPA calculations, we also distribute the integration points on the real or imaginary axes.

D. Computational Details

We consider four representative solids with different electronic properties and structural characteristics: diamond as an example of a wide-bandgap semiconductor, carbon dioxide (CO_2) as a representative molecular crystal with weak intermolecular interactions, nickel monoxide (NiO) as a correlated transition metal oxide exhibiting Mott insulating behavior, and the infinite-layer CaCuO_2 (CCO) as a prototypical cuprate superconductor material with a layered perovskite structure.

All calculations were performed on Intel IceLake 8352Y processors (32-core, 2.2 GHz) with parallelization. For all systems, we employed correlation-consistent GTH-cc-pVDZ Gaussian basis sets [103] and the Goedecker-Teter-Hutter family of pseudopotentials specifically optimized for Hartree-Fock calculations [104–106]. For Brillouin zone sampling, Γ -centered \mathbf{k} -point meshes were utilized, and all mean-field calculations were converged to an accuracy of 10^{-6} a.u. per unit cell. To address the integrable divergence of exact exchange, we applied the leading-order exchange finite-size correction (probe-charge Ewald, `exxdiv=ewald` in PySCF) [92, 107]. For the correlated wavefunction solver, we used coupled cluster singles and doubles (CCSD) as well as with perturbative triples (CCSD(T)) as implemented in PySCF [93, 94]. The DMET calculations were conducted using the interacting bath approach with correlation-potential fitting, but without charge self-consistency (IB w/o CSC in Ref. [50]), utilizing a modified version of the LIBD-MET package. The LNO-based local correlation calculations were carried out through a module implemented in PySCF-FORGE [48], utilizing the cluster-specific bath natural orbitals (CBNO) scheme [108].

To establish optimal FFTISDF parameters, we implemented a systematic convergence procedure. Initially, reference Hartree-Fock calculations in the Gaussian-Plane-Wave framework were performed for a series of \mathbf{k} -point meshes, progressively increasing the plane-wave cutoff energy E_{cut} until the energy per atom (for all meshes) achieved convergence within a threshold of ϵ_1 .

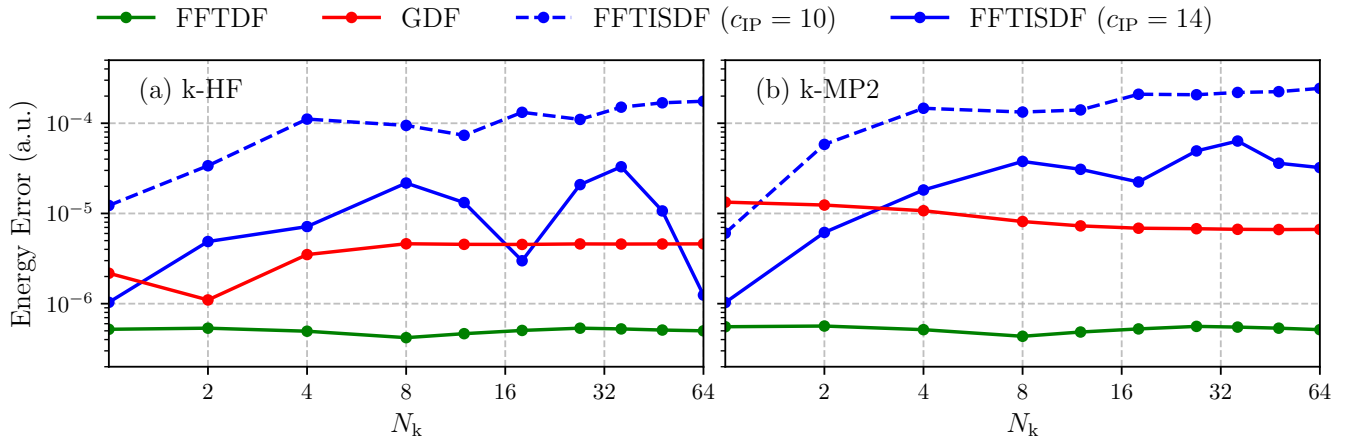


FIG. 1. Per-atom energy errors for diamond obtained with: FFTDF ($E_{\text{cut}} = 60$ a.u., green), GDF ($\beta = 2.0$, red), and FFTISDF ($E_{\text{cut}} = 60$ a.u., blue). For FFTISDF, results are shown for $c_{\text{IP}} = 10$ (dashed) and $c_{\text{IP}} = 14$ (solid). Errors are computed with respect to a reference FFTDF calculation ($E_{\text{cut}} = 160$ a.u.). Subfigures correspond to (a) k-HF and (b) k-MP2.

Subsequently, this converged E_{cut} value was used as the standard for both FFTDF and FFTISDF calculations. Building upon this, the FFTISDF calculations employ the established E_{cut} , whereas the interpolation point scaling factor c_{IP} was systematically adjusted to maintain accuracy relative to the FFTDF reference within a threshold of ϵ_2 for both k-HF and k-MP2. Additionally, Gaussian density fitting (GDF) was used as an alternative reference method, implemented with even-tempered auxiliary basis sets using an exponent parameter $\beta = 2.0$. Meanwhile, additional parameters specific to the DMET and LNO calculations were established following recommendations from Ref. [50] and Ref. [48].

The optimized parameters for each system are summarized in Table I, with convergence thresholds set to $\epsilon_1 = 10^{-6}$ a.u. per atom and $\epsilon_2 = 10^{-4}$ a.u. per atom.

TABLE I. Number of atoms, number of atomic orbitals and chosen computational parameters for the GTH-cc-pVQZ basis.

System	N_{atom}	N_{AO}	E_{cut} (a.u.)	c_{IP}
Diamond	2	26	60.0	14.0
CO_2	12	156	140.0	14.0
NiO (AFM cell)	4	78	180.0	25.0
CCO (2×2 cell)	16	308	180.0	25.0

III. RESULTS AND DISCUSSION

A. Diamond

We begin by assessing the accuracy and efficiency of FFTISDF using the diamond crystal as a benchmark. To ensure a rigorous comparison, we evaluated the ground-state energies (at both k-HF and k-MP2 levels) and the wall times for each computational step against established density fitting schemes (FFTDF and Gaussian Density Fitting (GDF)). This consistent setup allows for a direct evaluation of performance across all methods. To avoid Laplace-transform integration grid errors, the k-MP2 calculations with FFTISDF were obtained here from the exact MP2 expression using the FFTISDF two-electron integrals. The per-atom energy deviations are summarized in Fig. 1, utilizing FFTDF with $E_{\text{cut}} = 160$ a.u. as the reference. For FFTDF ($E_{\text{cut}} = 60$ a.u.), the error remains small ($< 10^{-6}$ a.u. per atom), confirming the cutoff's sufficiency. Similarly, GDF yields consistent errors of approximately 10^{-5} a.u. per atom, independent of the mesh size.

The FFTISDF accuracy clearly depends on both c_{IP} and the number of k-points. With $c_{\text{IP}} = 10$, the error increases initially but approaches an asymptotic limit of approximately 10^{-3} a.u. for $N_k > 8$. The accuracy is systematically improved by increasing the interpolation point scaling factor. When $c_{\text{IP}} = 14$, the per-atom error is systematically reduced to below 10^{-4} a.u.. Consequently, we employ $E_{\text{cut}} = 60$ a.u. and $c_{\text{IP}} = 14$ (as detailed in Table I) for all subsequent calculations.

Next, we evaluate the computational efficiency by analyzing the wall times required for computing integrals, Coulomb matrices, exchange matrices, and the fragment Hamiltonian. The results are plotted against the number of k-points in Fig. 2, with solid lines indicating the scaling

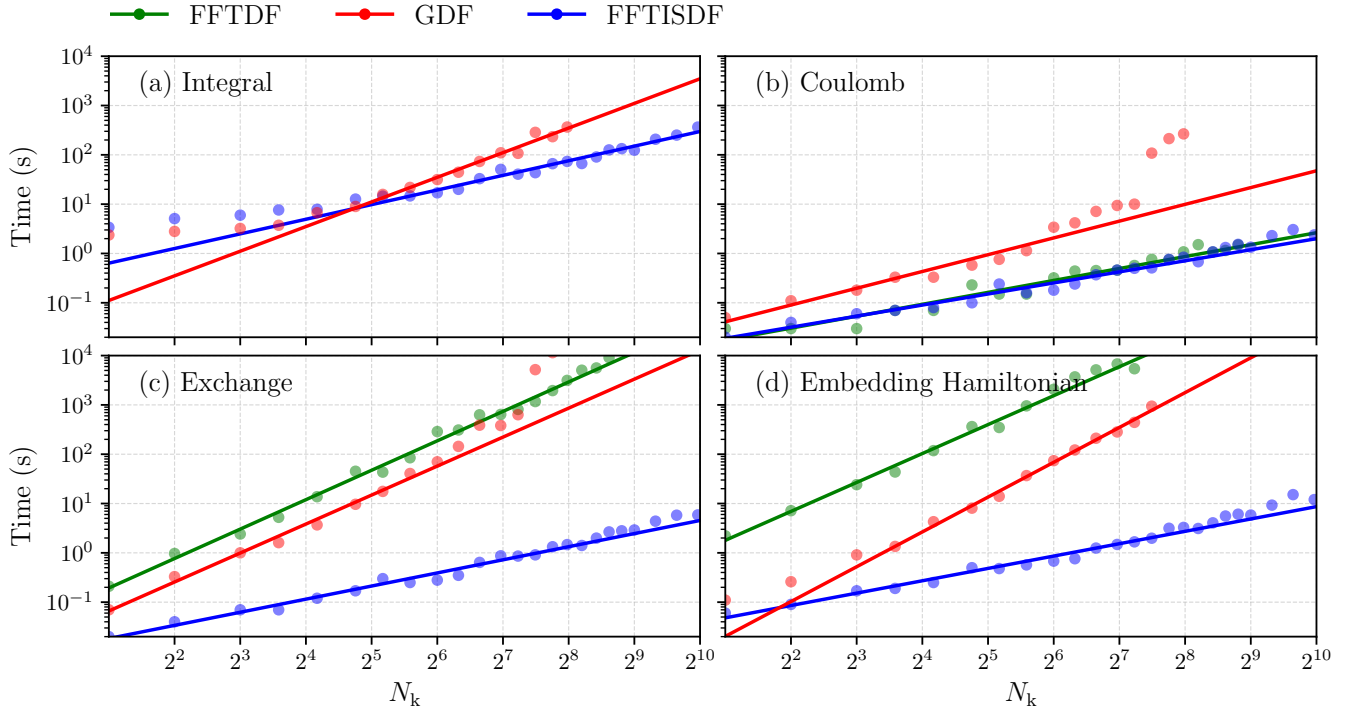


FIG. 2. Comparison of wall-clock times for different density-fitting schemes applied to the diamond system, plotted against the number of k-points (N_k). Panels show the timing for: (a) integral evaluation, (b) Coulomb matrix construction, (c) exchange matrix construction, and (d) embedding Hamiltonian construction. Solid lines indicate fitted trends highlighting the computational scaling (linear or quadratic) of each method.

TABLE II. Convergence of ground state and correlation energies (in a.u. per atom) for diamond with respect to k-point sampling. The second column reports the k-HF energy, while columns 3–8 present correlation energies obtained from DMET (with CCSD solver), k-SOS-MP2, k-dRPA, LNO-MP2, LNO-CCSD, and LNO-CCSD(T). The LNO-based methods are extrapolated to the full correlation domain using k-SOS-MP2 as a baseline. The bottom row shows values extrapolated to TDL.

N_k	E (a.u.)	E_{corr} (a.u.)					
		DMET	k-SOS-MP2	k-dRPA	LNO-MP2	LNO-CCSD	LNO-CCSD(T)
$2 \times 2 \times 2$	-5.4786	-0.0814	-0.1112	-0.1269	-0.1174	-0.1237	-0.1292
$3 \times 3 \times 3$	-5.5111	-0.0897	-0.1169	-0.1321	-0.1257	-0.1316	-0.1364
$4 \times 4 \times 4$	-5.5144	-0.0938	-0.1196	-0.1342	-0.1299	-0.1343	-0.1395
$5 \times 5 \times 5$	-5.5142	-0.0960	-0.1208	-0.1351	-0.1316	-0.1355	-0.1408
$6 \times 6 \times 6$	-5.5137	-0.0975	-0.1213	-0.1355	-0.1323	-0.1361	-0.1414
$7 \times 7 \times 7$	-5.5134	-0.0984	-0.1216	-0.1357	-0.1326	-0.1363	-0.1416
$8 \times 8 \times 8$	-5.5131	-0.0992	-0.1217	-0.1358	-0.1328	-0.1364	-0.1418
$10 \times 10 \times 10$	-5.5129	-0.1002	-0.1218	-0.1359	—	—	—
TDL	-5.5127	-0.1010	-0.1219	-0.1361	-0.1331	-0.1367	-0.1421

behavior. As shown in Fig. 2(a), the integral calculation time for GDF shifts from linear to quadratic scaling as N_k increases. This change occurs as the computational bottleneck moves from the Cholesky decomposition of 2c2e integrals to the evaluation of 3c2e integrals. In contrast, FFTISDF maintains strict linear scaling across the entire range. While GDF is slightly faster at small N_k (below

2^5), FFTISDF outperforms it significantly as the system size grows. Note that FFTDF is excluded from this comparison as it avoids the computation of intermediate integrals.

For the Coulomb matrix evaluation [Fig. 2(b)], while all schemes scale linearly, GDF incurs a notably higher computational cost compared to FFTDF and FFTISDF.

For exchange matrices [Fig. 2(c)], despite avoiding intermediate integral computations, FFTDF exhibits quadratic scaling and remains the most computationally expensive method. GDF also displays quadratic scaling, whereas FFTISDF is the only method that preserves linear scaling, demonstrating superior efficiency. This advantage extends to the construction of the fragment Hamiltonian [Fig. 2(d)]. As FFTDF and GDF scale quadratically, they rapidly become computationally prohibitive. In contrast, FFTISDF preserves linear scaling, offering a speedup of several orders of magnitude at large N_k and enabling efficient quantum embedding and local correlation calculations for up to 1000 k-points.

Beyond computational time, FFTISDF also offers superior storage efficiency to GDF, scaling as $N_k N_{IP}^2 + N_k N_{IP} N_{AO}$, in contrast to $N_k^2 N_{AO}^2 N_{aux}$ for GDF. This improvement results in a significant reduction in storage requirements, from 881.09 GB to 2.11 GB in the 1000 k-point diamond case.

We next extrapolate the FFTISDF results to the thermodynamic limit. Table II presents the per-atom k-HF energies and correlation energies from DMET, k-SOS-MP2, LNO-MP2, k-dRPA, LNO-CCSD, and LNO-CCSD(T) calculated for a series of cubic k-point meshes. To reduce the computational cost of LNO calculations for large correlation domains, we used k-SOS-MP2 energies to extrapolate the LNO-CCSD and LNO-CCSD(T) energies (details provided in the following subsection). The thermodynamic limit is then obtained by performing a linear fit against N_k^{-1} using data from the four largest k-point meshes, as the Ewald exchange divergence correction ensures $\mathcal{O}(N_k^{-1})$ convergence behavior. The extrapolation is visualized in Fig. 4.

Notably, as more k-points are systematically incorporated, the k-HF energy initially decreases and then gradually increases before finally approaching the TDL value. While previously reported [109], this energy-increasing regime remains prohibitive to sample adequately using existing methods (FFTDF and GDF) due to their steep scaling. Consequently, TDL extrapolations based on such truncated data are inherently less reliable. For correlated methods, DMET substantially underestimates the correlation energy as a result of its restricted embedding space size, whereas the other correlated approaches yield more consistent values. Finally, the efficiency of FFTISDF makes it possible to extrapolate to reliable CCSD(T) energies at the thermodynamic limit for diamond.

B. Carbon dioxide

We select the carbon dioxide system as a representative molecular crystal, and to demonstrate the extrapolation procedure to the complete correlation domain. Initially, k-HF calculations were performed using the exchange matrix defined by Eq. 10. Subsequently, the k-SOS-MP2 correlation energy was evaluated using Eq. 11, establishing the reference point for the extrapolation.

Following this, LNO computations were performed across a range of truncation thresholds to obtain SOS-MP2, MP2, CCSD, and CCSD(T) correlation energies for each domain size. The difference between k-SOS-MP2 and LNO-SOS-MP2 correlation energies is denoted as Δ_{LNO} . The MP2, CCSD, and CCSD(T) energies from the four largest correlation domains were then linearly fitted as functions of the corresponding Δ_{LNO} values.

Finally, by extrapolating to $\Delta_{LNO} = 0$ (corresponding to the complete k-SOS-MP2 limit), the global MP2, CCSD, and CCSD(T) correlation energies were obtained. This framework enables efficient evaluation of global correlation energies without incurring the prohibitive computational costs associated with direct large-scale calculations.

To validate the accuracy of our extrapolation procedure, we analyze the relationship between the LNO-SOS-MP2 correlation energies and their LNO-MP2, LNO-CCSD, and LNO-CCSD(T) counterparts across varying correlation domain sizes. Fig. 3(a) illustrates the results for a $1 \times 1 \times 1$ k-point mesh (Γ -point), where the small circles denote the LNO energies and triangles represent the corresponding global k-point reference values. As expected, as the correlation domain expands, all LNO correlation energies (circles) systematically converge toward their global counterparts (triangles), confirming the correct asymptotic behavior. Based on this trend, we performed the extrapolation, with both the fitted lines and the resulting extrapolated values (crosses) displayed in the figure. The LNO-MP2 data points exhibit near-perfect linear alignment, resulting in exceptional agreement between the extrapolated value ($E_{corr}^{LNO-MP2} = -1.8519$ a.u.) and the global reference ($E_{corr}^{k-MP2} = -1.8517$ a.u.). The corresponding per-atom error is $\sim 1 \times 10^{-5}$ a.u.

The CCSD and CCSD(T) data show slight deviations from the fitted line for the small domains. This leads to minor differences between the extrapolated values ($E_{corr}^{LNO-CCSD} = -1.8710$ a.u.; $E_{corr}^{LNO-CCSD(T)} = -1.9405$ a.u.) and their global references ($E_{corr}^{k-CCSD} = -1.8703$ a.u.; $E_{corr}^{k-CCSD(T)} = -1.9398$ a.u.). Nevertheless, these errors remain remarkably small, with per-atom errors of $\sim 6 \times 10^{-5}$ a.u. in both cases.

We subsequently extended the extrapolation procedure to larger k-point meshes, specifically the $2 \times 2 \times 2$ and $4 \times 4 \times 4$ configurations, as illustrated in Fig. 3(b) and (c). Although reference data is limited to k-MP2 for the $2 \times 2 \times 2$ mesh and is unavailable for other cases due to prohibitive computational costs, the overall trends remain consistent with those observed at the Γ -point. Notably, we observe a substantial gap between the LNO-SOS-MP2 energy (using the largest affordable domain) and the exact global k-SOS-MP2 reference. At the $2 \times 2 \times 2$ mesh, this deviation amounts to $\sim 1 \times 10^{-3}$ a.u. per atom ($E_{corr}^{k-SOS-MP2} = -1.7750$ a.u. and $E_{corr}^{LNO-SOS-MP2} = -1.7582$ a.u.). A similar discrepancy is found in the MP2 correlation energy ($\sim 2 \times 10^{-3}$ a.u. per atom; $E_{corr}^{k-MP2} = -1.8956$ a.u. and

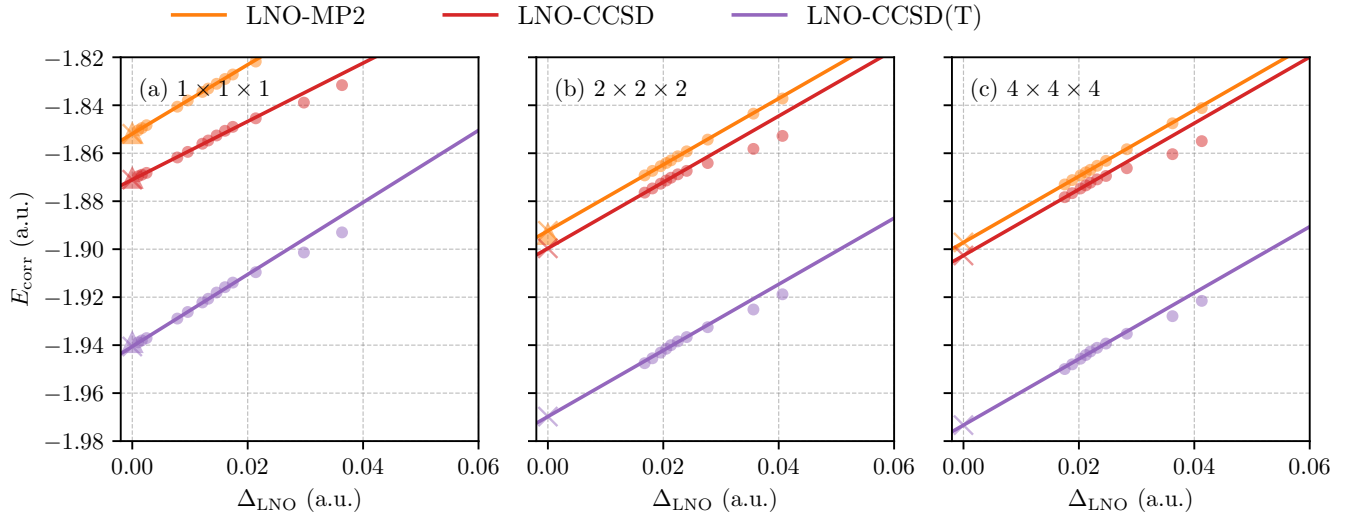


FIG. 3. Extrapolation of CO_2 correlation energies. LNO-MP2, LNO-CCSD, and LNO-CCSD(T) correlation energies plotted against Δ_{LNO} (the difference between k-SOS-MP2 and LNO-SOS-MP2 correlation energies) for k-point meshes: (a) $1 \times 1 \times 1$ (Γ -point only), (b) $2 \times 2 \times 2$, and (c) $4 \times 4 \times 4$. Small circles represent LNO correlation energies, triangles show global k-point counterparts, crosses mark extrapolated values, and solid lines are fitted lines.

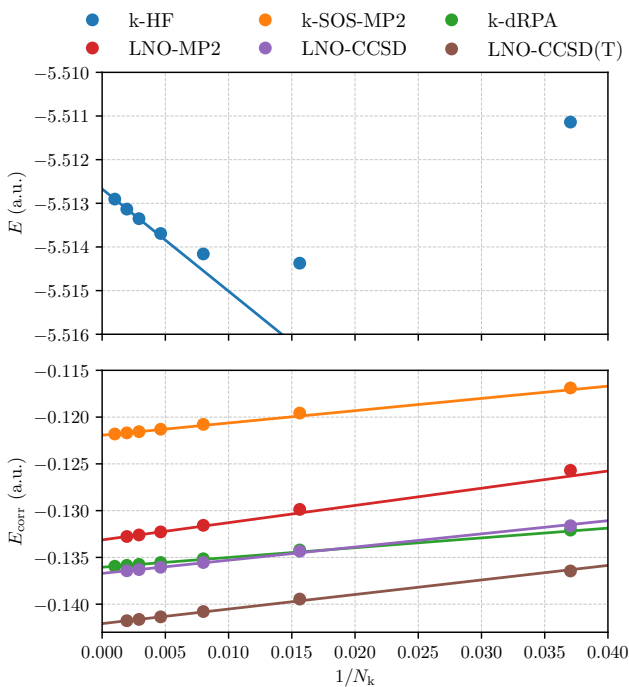


FIG. 4. Thermodynamic limit extrapolation for diamond. Upper panel: k-HF total energy as a function of $1/N_k$. Lower panel: correlation energies from various methods including k-SOS-MP2, LNO-MP2, k-dRPA, LNO-CCSD, and LNO-CCSD(T). Solid lines represent linear fits used for extrapolation to the thermodynamic limit ($1/N_k \rightarrow 0$).

$E_{\text{corr}}^{\text{LNO-MP2}} = -1.8707$ a.u.). However, the extrapolation reduces the error to $\sim 1 \times 10^{-4}$ a.u. per atom. This result

highlights the insufficiency of the computationally accessible truncated domains and establishes the effectiveness of our extrapolation strategy. Although global correlated benchmarks are unavailable for the larger k-point meshes, the LNO-based methods continue to exhibit excellent linearity. Consequently, we anticipate high reliability for the extrapolated values derived from these linear extrapolations.

TABLE III. Extrapolated TDL energies for HF, MP2, CCSD, and CCSD(T) for CO_2 .

Method	E_{corr} (a.u.)	E (a.u.)
HF	—	-148.0545
MP2	-1.8979	-149.9524
CCSD	-1.9030	-149.9574
CCSD(T)	-1.9748	-150.0293

Based on the validation of the LNO-extrapolation procedure, we further proceeded to obtain the total energies in the TDL by employing multiple k-point meshes. The final values are summarized in Table III.

C. Nickel monoxide and cuprate

We apply the FFTISDF-DMET framework with a CCSD solver to two prototypical strongly correlated transition metal oxides: NiO and CaCuO_2 (CCO). Our analysis focuses on the energy difference between antiferromagnetic (AFM) and ferromagnetic (FM) orderings. Notably, the implementation of such large k-point meshes

TABLE IV. Ground-state energies (in a.u.) and Heisenberg exchange constants J (in meV) for NiO and CCO in the AFM and FM states, calculated using k-HF and DMET (CCSD solver) with various k-point meshes. The thermodynamic limit (TDL) is obtained by extrapolating the k-HF energies and DMET correlation energies separately using a linear fit against N_k^{-1} with the three largest k-point grids. J represents the next-nearest-neighbor exchange constant J_2 for NiO and the nearest-neighbor exchange constant J_1 for CCO.

N_k	E_{AFM} (a.u.)		E_{FM} (a.u.)		J (meV)	
	k-HF	DMET	k-HF	DMET	k-HF	DMET
NiO						
$2 \times 2 \times 2$	-366.7825	-367.3968	-366.7794	-367.3918	-14.10	-22.88
$3 \times 3 \times 3$	-366.7687	-367.3778	-366.7669	-367.3744	-8.12	-15.75
$4 \times 4 \times 4$	-366.7622	-367.3766	-366.7605	-367.3734	-7.69	-14.75
$5 \times 5 \times 5$	-366.7593	-367.3770	-366.7576	-367.3738	-7.63	-14.09
$6 \times 6 \times 6$	-366.7580	-367.3785	-366.7563	-367.3753	-7.63	-14.43
TDL	-366.7562	-367.3787	-366.7545	-367.3756	-7.59	-14.05
CCO						
$2 \times 2 \times 1$	-1055.4085	-1056.5605	-1055.4012	-1056.5342	-50.02	-178.69
$4 \times 4 \times 2$	-1053.5604	-1054.5908	-1053.5545	-1054.5663	-40.35	-167.10
$6 \times 6 \times 4$	-1050.5774	-1051.6032	-1050.5715	-1051.5783	-40.66	-169.14
TDL	-1053.2964	-1054.3095	-1053.2907	-1054.2851	-38.97	-165.44

is made feasible specifically by the FFTISDF algorithm. This allows us to systematically study long-range correlation effects that are critical for accurately determining the magnetic energy gaps in the strongly correlated regime.

When NiO is cooled below its Néel temperature, it adopts an AFM phase characterized by staggered magnetization along the [111] direction, commonly known as the AFM-II phase. By mapping the energy difference between the AFM and FM states to a spin Hamiltonian, one can derive the nearest-neighbor J_1 and next-nearest-neighbor J_2 exchange constants [110]. Since experimental and theoretical evidence indicates that J_1 is negligible in NiO [111], we neglect its contribution and focus exclusively on computing J_2 , the dominant exchange interaction, from the difference in the FM and AFM energies.

Table IV presents the ground-state energies obtained from k-HF and DMET calculations across various k-point meshes, using spin-polarized initial guesses. To approach the thermodynamic limit, we extrapolated the k-HF energies and DMET correlation energies separately by performing a linear fit against N_k^{-1} using data from the three largest k-point meshes. The extrapolation reveals distinct behaviors between the two methods. While k-HF systematically underestimates J_2 , DMET yields a value of -14.05 meV, slightly underestimating the magnitude compared to the experimental range of -19.8 to -17.0 meV [112]. This improvement over k-HF demonstrates the importance of incorporating correlation effects in describing the magnetic interactions of NiO.

Turning to CCO, the defining structural feature of this

cuprate compound is the two-dimensional CuO_2 square lattice plane (formally $[\text{CuO}_2]^{2-}$). While these planes are typically separated by buffer layers in various high- T_c families, we focus here on the infinite-layer calcium cuprate CaCuO_2 . Due to the layered structure, we employ anisotropic k-point meshes with fewer points along the c -axis. The correlation effects in CCO are even more pronounced than in NiO. At the thermodynamic limit, DMET yields $J = -165.44$ meV, more than four times larger in magnitude than the k-HF value of -38.97 meV. This DMET result is in good agreement with experimental values of -142 and -158 meV obtained by fitting the spin-wave dispersion near the Γ point [113, 114].

IV. CONCLUSION

We have described an implementation of interpolative separable density fitting in the Gaussian-Plane-Wave framework (FFTISDF in PySCF) and its integration with quantum embedding and local correlation frameworks. This implementation establishes a robust computational framework capable of obtaining converged ground-state energies from DMET and LNO-based MP2, CCSD, and CCSD(T) calculations for crystals with simple unit cells in the thermodynamic limit. While this efficient methodology opens new avenues for high-level correlated calculations in extended systems, several aspects of the proposed approach still warrant further improvement.

First, the current implementation requires a relatively

large number of interpolation points, typically ten times the number of atomic orbitals (see Table I), to reach our desired accuracy. As a result, the determination of these interpolation points becomes computationally demanding, particularly for systems with large unit cells. Developing efficient protocols for generating compact interpolation points would therefore be highly desirable.

Second, the size of the real-space grid employed in the fast Fourier transforms remains large. This is a challenge for systems containing transition metals or those with large unit cells.

Finally, in this work, LNO-based approaches employed the CBNO scheme [108] for constructing correlation domains, although this method does not exhibit an optimal convergence with respect to the domain size [48]. Exploring alternative correlating spaces is of interest. Further-

more, the developed embedding framework can be readily extended to other quantum embedding approaches, such as dynamical mean field theory [43, 53].

V. ACKNOWLEDGEMENTS

This work was supported by the U.S. Department of Energy, Office of Science, through Award No. DE-SC0018140. G.K.C. is a Simons Investigator in Physics. We are grateful to Zhi-hao Cui and Shuoxue Li for their assistance with the DMET calculations. We thank Rui Li, Xing Zhang, Ruiheng Song, and Yao Luo for insightful discussions. The code and data for this work are available at <https://github.com/yangjunjie0320/fftisdf>.

[1] M. Marsman, A. Grüneis, J. Paier, and G. Kresse, Second-order Møller–Plesset perturbation theory applied to extended systems. I. Within the projector-augmented-wave formalism using a plane wave basis set, *The Journal of Chemical Physics* **130**, 184103 (2009).

[2] C. Müller and B. Paulus, Wavefunction-based electron correlation methods for solids, *Phys. Chem. Chem. Phys.* **14**, 7605 (2012).

[3] G. H. Booth, A. Grüneis, G. Kresse, and A. Alavi, Towards an exact description of electronic wavefunctions in real solids, *Nature* **493**, 365 (2013).

[4] J. Yang, W. Hu, D. Usvyat, D. Matthews, M. Schütz, and G. K.-L. Chan, Ab initio determination of the crystalline benzene lattice energy to sub-kilojoule/mole accuracy, *Science* **345**, 640 (2014).

[5] A. Kubas, D. Berger, H. Oberhofer, D. Maganas, K. Reuter, and F. Neese, Surface Adsorption Energetics Studied with “Gold Standard” Wave-Function-Based Ab Initio Methods: Small-Molecule Binding to TiO₂ (110), *J. Phys. Chem. Lett.* **7**, 4207 (2016).

[6] J. McClain, Q. Sun, G. K.-L. Chan, and T. C. Berkelbach, Gaussian-Based Coupled-Cluster Theory for the Ground-State and Band Structure of Solids, *J. Chem. Theory Comput.* **13**, 1209 (2017).

[7] T. Gruber, K. Liao, T. Tsatsoulis, F. Hummel, and A. Grüneis, Applying the Coupled-Cluster Ansatz to Solids and Surfaces in the Thermodynamic Limit, *Phys. Rev. X* **8**, 021043 (2018).

[8] I. Y. Zhang and A. Grüneis, Coupled Cluster Theory in Materials Science, *Front. Mater.* **6**, 123 (2019).

[9] J. Sauer, Ab Initio Calculations for Molecule–Surface Interactions with Chemical Accuracy, *Acc. Chem. Res.* **52**, 3502 (2019).

[10] R. Dovesi, F. Pascale, B. Civalleri, K. Doll, N. M. Harrison, I. Bush, P. D’Arco, Y. Noël, M. Rérat, P. Carbone, M. Causà, S. Salustro, V. Lacivita, B. Kirtman, A. M. Ferrari, F. S. Gentile, J. Baima, M. Ferrero, R. Demichelis, and M. De La Pierre, The CRYSTAL code, 1976–2020 and beyond, a long story, *The Journal of Chemical Physics* **152**, 204111 (2020).

[11] B. X. Shi, A. Zen, V. Kapil, P. R. Nagy, A. Grüneis, and A. Michaelides, Many-Body Methods for Surface Chemistry Come of Age: Achieving Consensus with Experiments, *J. Am. Chem. Soc.* **145**, 25372 (2023).

[12] K. Raghavachari, G. W. Trucks, J. A. Pople, and M. Head-Gordon, A fifth-order perturbation comparison of electron correlation theories, *Chemical Physics Letters* **157**, 479 (1989).

[13] T. D. Crawford and H. F. Schaefer, An Introduction to Coupled Cluster Theory for Computational Chemists, in *Reviews in Computational Chemistry*, Vol. 14, edited by K. B. Lipkowitz and D. B. Boyd (Wiley, 2000) 1st ed., pp. 33–136.

[14] R. J. Bartlett and M. Musiał, Coupled-cluster theory in quantum chemistry, *Rev. Mod. Phys.* **79**, 291 (2007).

[15] M. Motta, S. Zhang, and G. K.-L. Chan, Hamiltonian symmetries in auxiliary-field quantum Monte Carlo calculations for electronic structure, *Physical Review B* **100**, 045127 (2019).

[16] P. Pulay, Localizability of dynamic electron correlation, *Chemical Physics Letters* **100**, 151 (1983).

[17] W. Kohn, Density Functional and Density Matrix Method Scaling Linearly with the Number of Atoms, *Phys. Rev. Lett.* **76**, 3168 (1996).

[18] K. B. Lipkowitz and T. R. Cundari, eds., *Reviews in Computational Chemistry*, 1st ed., Reviews in Computational Chemistry, Vol. 23 (Wiley, 2007).

[19] S. Li, J. Ma, and Y. Jiang, Linear scaling local correlation approach for solving the coupled cluster equations of large systems, *J Comput Chem* **23**, 237 (2002).

[20] S. Li, J. Shen, W. Li, and Y. Jiang, An efficient implementation of the “cluster-in-molecule” approach for local electron correlation calculations, *The Journal of Chemical Physics* **125**, 074109 (2006).

[21] Z. Rolik and M. Kállay, A general-order local coupled-cluster method based on the cluster-in-molecule approach, *The Journal of Chemical Physics* **135**, 104111 (2011).

[22] Z. Rolik, L. Szegedy, I. Ladjánszki, B. Ladóczki, and M. Kállay, An efficient linear-scaling CCSD(T) method based on local natural orbitals, *The Journal of Chemical Physics* **139**, 094105 (2013).

[23] W. Li, Z. Ni, and S. Li, Cluster-in-molecule local correlation method for post-Hartree–Fock calculations of

large systems, *Molecular Physics* **114**, 1447 (2016).

[24] C. Hampel and H.-J. Werner, Local treatment of electron correlation in coupled cluster theory, *The Journal of Chemical Physics* **104**, 6286 (1996).

[25] C. Hättig, D. P. Tew, and B. Helmich, Local explicitly correlated second- and third-order Møller–Plesset perturbation theory with pair natural orbitals, *The Journal of Chemical Physics* **136**, 204105 (2012).

[26] C. Riplinger and F. Neese, An efficient and near linear scaling pair natural orbital based local coupled cluster method, *The Journal of Chemical Physics* **138**, 034106 (2013).

[27] M. Schwick, Q. Ma, C. Köppl, and H.-J. Werner, Scalable Electron Correlation Methods. 3. Efficient and Accurate Parallel Local Coupled Cluster with Pair Natural Orbitals (PNO-LCCSD), *J. Chem. Theory Comput.* **13**, 3650 (2017).

[28] Y. Guo, C. Riplinger, U. Becker, D. G. Liakos, Y. Minenkov, L. Cavallo, and F. Neese, Communication: An improved linear scaling perturbative triples correction for the domain based local pair-natural orbital based singles and doubles coupled cluster method [DLPNO-CCSD(T)], *The Journal of Chemical Physics* **148**, 011101 (2018).

[29] M. Ziolkowski, B. Jansik, T. Kjærgaard, and P. Jørgensen, Linear scaling coupled cluster method with correlation energy based error control, *The Journal of Chemical Physics* **133**, 014107 (2010).

[30] K. Kristensen, I.-M. Høyvik, B. Jansik, P. Jørgensen, T. Kjærgaard, S. Reine, and J. Jakowski, MP2 energy and density for large molecular systems with internal error control using the Divide-Expand-Consolidate scheme, *Phys. Chem. Chem. Phys.* **14**, 15706 (2012).

[31] P. Y. Ayala and G. E. Scuseria, Linear scaling second-order Moller–Plesset theory in the atomic orbital basis for large molecular systems, *The Journal of Chemical Physics* **110**, 3660 (1999).

[32] G. E. Scuseria and P. Y. Ayala, Linear scaling coupled cluster and perturbation theories in the atomic orbital basis, *The Journal of Chemical Physics* **111**, 8330 (1999).

[33] T. A. Wesolowski and A. Warshel, Frozen density functional approach for ab initio calculations of solvated molecules, *J. Phys. Chem.* **97**, 8050 (1993).

[34] J. D. Goodpaster, N. Ananth, F. R. Manby, and T. F. Miller, Exact nonadditive kinetic potentials for embedded density functional theory, *The Journal of Chemical Physics* **133**, 084103 (2010).

[35] C. Huang, M. Pavone, and E. A. Carter, Quantum mechanical embedding theory based on a unique embedding potential, *The Journal of Chemical Physics* **134**, 154110 (2011).

[36] F. Libisch, C. Huang, and E. A. Carter, Embedded Correlated Wavefunction Schemes: Theory and Applications, *Acc. Chem. Res.* **47**, 2768 (2014).

[37] H.-Z. Ye, H. K. Tran, and T. Van Voorhis, Bootstrap Embedding For Large Molecular Systems, *J. Chem. Theory Comput.* **16**, 5035 (2020).

[38] M. Nusspickel and G. H. Booth, Systematic Improvability in Quantum Embedding for Real Materials, *Phys. Rev. X* **12**, 011046 (2022).

[39] A. Shee, F. M. Faulstich, K. B. Whaley, L. Lin, and M. Head-Gordon, A static quantum embedding scheme based on coupled cluster theory, *The Journal of Chemical Physics* **161**, 164107 (2024).

[40] E. Rebolini, G. Baardsen, A. S. Hansen, K. R. Leikanger, and T. B. Pedersen, Divide–Expand–Consolidate Second-Order Møller–Plesset Theory with Periodic Boundary Conditions, *J. Chem. Theory Comput.* **14**, 2427 (2018).

[41] Y. Wang, Z. Ni, W. Li, and S. Li, Cluster-in-Molecule Local Correlation Approach for Periodic Systems, *J. Chem. Theory Comput.* **15**, 2933 (2019).

[42] S. J. R. Lee, M. Welborn, F. R. Manby, and T. F. Miller, Projection-Based Wavefunction-in-DFT Embedding, *Acc. Chem. Res.* **52**, 1359 (2019).

[43] T. Zhu, Z.-H. Cui, and G. K.-L. Chan, Efficient Formulation of Ab Initio Quantum Embedding in Periodic Systems: Dynamical Mean-Field Theory, *J. Chem. Theory Comput.* **16**, 141 (2020).

[44] Y. Wang, Z. Ni, F. Neese, W. Li, Y. Guo, and S. Li, Cluster-in-Molecule Method Combined with the Domain-Based Local Pair Natural Orbital Approach for Electron Correlation Calculations of Periodic Systems, *J. Chem. Theory Comput.* **18**, 6510 (2022).

[45] B. Chen and X. Xu, XO-PBC: An Accurate and Efficient Method for Molecular Crystals, *J. Chem. Theory Comput.* **16**, 4271 (2020).

[46] O. R. Meitei and T. Van Voorhis, Periodic Bootstrap Embedding, *J. Chem. Theory Comput.* **19**, 3123 (2023).

[47] W. Li, Y. Wang, Z. Ni, and S. Li, Cluster-in-Molecule Local Correlation Method for Dispersion Interactions in Large Systems and Periodic Systems, *Acc. Chem. Res.* **56**, 3462 (2023).

[48] H.-Z. Ye and T. C. Berkelbach, Periodic Local Coupled-Cluster Theory for Insulators and Metals, *J. Chem. Theory Comput.* **20**, 8948 (2024).

[49] Z.-H. Cui, C. Sun, U. Ray, B.-X. Zheng, Q. Sun, and G. K.-L. Chan, Ground-state phase diagram of the three-band Hubbard model from density matrix embedding theory, *Phys. Rev. Research* **2**, 043259 (2020).

[50] Z.-H. Cui, T. Zhu, and G. K.-L. Chan, Efficient Implementation of Ab Initio Quantum Embedding in Periodic Systems: Density Matrix Embedding Theory, *J. Chem. Theory Comput.* **16**, 119 (2020).

[51] Z.-H. Cui, H. Zhai, X. Zhang, and G. K.-L. Chan, Systematic electronic structure in the cuprate parent state from quantum many-body simulations, *Science* **377**, 1192 (2022).

[52] Z.-H. Cui, J. Yang, J. Tölle, H.-Z. Ye, S. Yuan, H. Zhai, G. Park, R. Kim, X. Zhang, L. Lin, T. C. Berkelbach, and G. K.-L. Chan, Ab initio quantum many-body description of superconducting trends in the cuprates, *Nat Commun* **16**, 1845 (2025).

[53] D. Zgid and G. K.-L. Chan, Dynamical mean-field theory from a quantum chemical perspective, *The Journal of Chemical Physics* **134**, 094115 (2011).

[54] Q. Sun and G. K.-L. Chan, Quantum Embedding Theories, *Acc. Chem. Res.* **49**, 2705 (2016).

[55] G. Knizia and G. K.-L. Chan, Density matrix embedding: A strong-coupling quantum embedding theory, *Journal of chemical theory and computation* **9**, 1428 (2013).

[56] S. Wouters, C. A. Jiménez-Hoyos, Q. Sun, and G. K.-L. Chan, A practical guide to density matrix embedding theory in quantum chemistry, *Journal of chemical theory and computation* **12**, 2706 (2016).

[57] S. Haldar, A. Mitra, M. R. Hermes, and L. Gagliardi, Local Excitations of a Charged Nitrogen Vacancy in Diamond with Multireference Density Matrix Embedding Theory, *J. Phys. Chem. Lett.* **14**, 4273 (2023).

[58] B. T. G. Lau, B. Busemeyer, and T. C. Berkelbach, Optical Properties of Defects in Solids via Quantum Embedding with Good Active Space Orbitals, *J. Phys. Chem. C* **128**, 2959 (2024).

[59] H. Q. Pham, M. R. Hermes, and L. Gagliardi, Periodic Electronic Structure Calculations with the Density Matrix Embedding Theory, *J. Chem. Theory Comput.* **16**, 130 (2020).

[60] B. T. G. Lau, G. Knizia, and T. C. Berkelbach, Regional Embedding Enables High-Level Quantum Chemistry for Surface Science, *J. Phys. Chem. Lett.* **12**, 1104 (2021).

[61] E. Baerends, D. Ellis, and P. Ros, Self-consistent molecular Hartree–Fock–Slater calculations I. The computational procedure, *Chemical Physics* **2**, 41 (1973).

[62] J. L. Whitten, Coulombic potential energy integrals and approximations, *The Journal of Chemical Physics* **58**, 4496 (1973).

[63] J. A. Jafri and J. L. Whitten, Electron repulsion integral approximations and error bounds: Molecular applications, *The Journal of Chemical Physics* **61**, 2116 (1974).

[64] N. H. F. Beebe and J. Linderberg, Simplifications in the generation and transformation of two-electron integrals in molecular calculations, *Int J of Quantum Chemistry* **12**, 683 (1977).

[65] I. Røeggen and E. Wisløff-Nilssen, On the Beebe–Linderberg two-electron integral approximation, *Chemical Physics Letters* **132**, 154 (1986).

[66] X. Ren, P. Rinke, V. Blum, J. Wieferink, A. Tkatchenko, A. Sanfilippo, K. Reuter, and M. Scheffler, Resolution-of-identity approach to Hartree–Fock, hybrid density functionals, RPA, MP2 and *GW* with numeric atom-centered orbital basis functions, *New J. Phys.* **14**, 053020 (2012).

[67] R. A. Friesner, Solution of self-consistent field electronic structure equations by a pseudospectral method, *Chemical Physics Letters* **116**, 39 (1985).

[68] F. Neese, F. Wennmohs, A. Hansen, and U. Becker, Efficient, approximate and parallel Hartree–Fock and hybrid DFT calculations. A ‘chain-of-spheres’ algorithm for the Hartree–Fock exchange, *Chemical Physics* **356**, 98 (2009).

[69] R. Izsák and F. Neese, An overlap fitted chain of spheres exchange method, *The Journal of Chemical Physics* **135**, 144105 (2011).

[70] E. G. Hohenstein, R. M. Parrish, and T. J. Martínez, Tensor hypercontraction density fitting. I. Quartic scaling second- and third-order Møller-Plesset perturbation theory, *The Journal of Chemical Physics* **137**, 044103 (2012).

[71] R. M. Parrish, E. G. Hohenstein, T. J. Martínez, and C. D. Sherrill, Tensor hypercontraction. II. Least-squares renormalization, *The Journal of Chemical Physics* **137**, 224106 (2012).

[72] C. Song and T. J. Martínez, Atomic orbital-based SOS-MP2 with tensor hypercontraction. I. GPU-based tensor construction and exploiting sparsity, *The Journal of Chemical Physics* **144**, 174111 (2016).

[73] D. A. Matthews, A critical analysis of least-squares tensor hypercontraction applied to MP3, *The Journal of Chemical Physics* **154**, 134102 (2021).

[74] W. Hu, L. Lin, and C. Yang, Interpolative Separable Density Fitting Decomposition for Accelerating Hybrid Density Functional Calculations with Applications to Defects in Silicon, *J. Chem. Theory Comput.* **13**, 5420 (2017).

[75] K. Dong, W. Hu, and L. Lin, Interpolative Separable Density Fitting through Centroidal Voronoi Tessellation with Applications to Hybrid Functional Electronic Structure Calculations, *J. Chem. Theory Comput.* **14**, 1311 (2018).

[76] X. Qin, J. Liu, W. Hu, and J. Yang, Interpolative Separable Density Fitting Decomposition for Accelerating Hartree–Fock Exchange Calculations within Numerical Atomic Orbitals, *J. Phys. Chem. A* **124**, 5664 (2020).

[77] X. Qin, J. Li, W. Hu, and J. Yang, Machine Learning K-Means Clustering Algorithm for Interpolative Separable Density Fitting to Accelerate Hybrid Functional Calculations with Numerical Atomic Orbitals, *J. Phys. Chem. A* **124**, 10066 (2020).

[78] S. Sharma, A. F. White, and G. Beylkin, Fast Exchange with Gaussian Basis Set Using Robust Pseudospectral Method, *J. Chem. Theory Comput.* **18**, 7306 (2022).

[79] K. E. Smyser, A. White, and S. Sharma, Use of Multi-grids to Reduce the Cost of Performing Interpolative Separable Density Fitting, *J. Phys. Chem. A* **128**, 7451 (2024).

[80] Z. Zhang, X. Yin, W. Hu, and J. Yang, Machine Learning K-Means Clustering of Interpolative Separable Density Fitting Algorithm for Accurate and Efficient Cubic-Scaling Exact Exchange Plus Random Phase Approximation within Plane Waves, *J. Chem. Theory Comput.* **20**, 1944 (2024).

[81] J. Lu and K. Thicke, Cubic scaling algorithms for RPA correlation using interpolative separable density fitting, *Journal of Computational Physics* **351**, 187 (2017).

[82] I. Duchemin and X. Blase, Separable resolution-of-the-identity with all-electron Gaussian bases: Application to cubic-scaling RPA, *The Journal of Chemical Physics* **150**, 174120 (2019).

[83] W. Gao and J. R. Chelikowsky, Accelerating Time-Dependent Density Functional Theory and *GW* Calculations for Molecules and Nanoclusters with Symmetry Adapted Interpolative Separable Density Fitting, *J. Chem. Theory Comput.* **16**, 2216 (2020).

[84] H. Ma, L. Wang, L. Wan, J. Li, X. Qin, J. Liu, W. Hu, L. Lin, C. Yang, and J. Yang, Realizing Effective Cubic-Scaling Coulomb Hole Plus Screened Exchange Approximation in Periodic Systems via Interpolative Separable Density Fitting with a Plane-Wave Basis Set, *J. Phys. Chem. A* **125**, 7545 (2021).

[85] I. Duchemin and X. Blase, Cubic-Scaling All-Electron *GW* Calculations with a Separable Density-Fitting Space–Time Approach, *J. Chem. Theory Comput.* **17**, 2383 (2021).

[86] F. D. Malone, S. Zhang, and M. A. Morales, Overcoming the Memory Bottleneck in Auxiliary Field Quantum Monte Carlo Simulations with Interpolative Separable Density Fitting, *J. Chem. Theory Comput.* **15**, 256 (2019).

[87] C.-N. Yeh and M. A. Morales, Low-Scaling Algorithm for the Random Phase Approximation Using Tensor Hypercontraction with k-Point Sampling, *J. Chem. Theory Comput.* **19**, 6197 (2023).

[88] C.-N. Yeh and M. A. Morales, Low-Scaling Algorithms for GW and Constrained Random Phase Approximation Using Symmetry-Adapted Interpolative Separable Density Fitting, *J. Chem. Theory Comput.* **20**, 3184 (2024).

[89] K. Wu, X. Qin, W. Hu, and J. Yang, Low-Rank Approximations Accelerated Plane-Wave Hybrid Functional Calculations with k-Point Sampling, *J. Chem. Theory Comput.* **18**, 206 (2022).

[90] X. Qin, W. Hu, and J. Yang, Interpolative Separable Density Fitting for Accelerating Two-Electron Integrals: A Theoretical Perspective, *J. Chem. Theory Comput.* **19**, 679 (2023).

[91] A. Rettig, J. Lee, and M. Head-Gordon, Even Faster Exact Exchange for Solids via Tensor Hypercontraction, *J. Chem. Theory Comput.* **19**, 5773 (2023).

[92] Q. Sun, T. C. Berkelbach, J. D. McClain, and G. K.-L. Chan, Gaussian and plane-wave mixed density fitting for periodic systems, *The Journal of Chemical Physics* **147**, 164119 (2017).

[93] Q. Sun, T. C. Berkelbach, N. S. Blunt, G. H. Booth, S. Guo, Z. Li, J. Liu, J. D. McClain, E. R. Sayfutyarova, S. Sharma, S. Wouters, and G. K.-L. Chan, PySCF: The Python-based simulations of chemistry framework, *WIREs Comput Mol Sci* **8**, e1340 (2018).

[94] Q. Sun, X. Zhang, S. Banerjee, P. Bao, M. Barbry, N. S. Blunt, N. A. Bogdanov, G. H. Booth, J. Chen, Z.-H. Cui, J. J. Eriksen, Y. Gao, S. Guo, J. Hermann, M. R. Hermes, K. Koh, P. Koval, S. Lehtola, Z. Li, J. Liu, N. Mardirossian, J. D. McClain, M. Motta, B. Mussard, H. Q. Pham, A. Pulkkin, W. Purwanto, P. J. Robinson, E. Ronca, E. R. Sayfutyarova, M. Scheurer, H. F. Schurkus, J. E. T. Smith, C. Sun, S.-N. Sun, S. Upadhyay, L. K. Wagner, X. Wang, A. White, J. D. Whitfield, M. J. Williamson, S. Wouters, J. Yang, J. M. Yu, T. Zhu, T. C. Berkelbach, S. Sharma, A. Y. Sokolov, and G. K.-L. Chan, Recent developments in the P Y SCF program package, *The Journal of Chemical Physics* **153**, 024109 (2020).

[95] D. A. Matthews, Improved Grid Optimization and Fitting in Least Squares Tensor Hypercontraction, *J. Chem. Theory Comput.* **16**, 1382 (2020).

[96] J. Lee, L. Lin, and M. Head-Gordon, Systematically Im- provable Tensor Hypercontraction: Interpolative Sep- arable Density-Fitting for Molecules Applied to Ex- act Exchange, Second- and Third-Order Møller-Plesset Perturbation Theory, *J. Chem. Theory Comput.* **16**, 243 (2020).

[97] F. Aryasetiawan, M. Imada, A. Georges, G. Kotliar, S. Biermann, and A. I. Lichtenstein, Frequency- dependent local interactions and low-energy effective models from electronic structure calculations, *Phys. Rev. B* **70**, 195104 (2004).

[98] Y. Chang, E. G. C. P. Van Loon, B. Eskridge, B. Buse- meyer, M. A. Morales, C. E. Dreyer, A. J. Millis, S. Zhang, T. O. Wehling, L. K. Wagner, and M. Rösner, Downfolding from ab initio to interacting model Hamil- tonians: Comprehensive analysis and benchmarking of the DFT+cRPA approach, *npj Comput Mater* **10**, 129 (2024).

[99] C. J. C. Scott and G. H. Booth, Rigorous Screened Inter- actions for Realistic Correlated Electron Systems, *Phys. Rev. Lett.* **132**, 076401 (2024).

[100] R. Song, X. Gong, A. Bakry, and H.-Z. Ye, Random phase approximation-based local natural orbital coupled cluster theory (2025), arXiv:2601.00131 [physics].

[101] A. Dixit, J. G. Ángyán, and D. Rocca, Improving the accuracy of ground-state correlation energies within a plane-wave basis set: The electron-hole exchange kernel, *The Journal of Chemical Physics* **145**, 104105 (2016).

[102] I. Haritan, X. Wang, and T. Goldzak, An Efficient Scaled Opposite-Spin MP2 Method for Periodic Sys- tems, *J. Chem. Theory Comput.* **21**, 6823 (2025).

[103] H.-Z. Ye and T. C. Berkelbach, Correlation-Consistent Gaussian Basis Sets for Solids Made Simple, *J. Chem. Theory Comput.* **18**, 1595 (2022).

[104] S. Goedecker, M. Teter, and J. Hutter, Separable dual- space Gaussian pseudopotentials, *Phys. Rev. B* **54**, 1703 (1996).

[105] C. Hartwigsen, S. Goedecker, and J. Hutter, Relativistic separable dual-space Gaussian pseudopotentials from H to Rn, *Phys. Rev. B* **58**, 3641 (1998).

[106] J. Hutter, GTH: GTH pseudopotentials for PBE, SCAN, PBE0, and Hartree-Fock, <https://github.com/juerghutter/GTH> (2024).

[107] R. Sundararaman and T. A. Arias, Regularization of the Coulomb singularity in exact exchange by Wigner-Seitz truncated interactions: Towards chemical accuracy in nontrivial systems, *Phys. Rev. B* **87**, 165122 (2013).

[108] M. Nusspickel, B. Ibrahim, and G. H. Booth, Effective Reconstruction of Expectation Values from Ab Initio Quantum Embedding, *J. Chem. Theory Comput.* **19**, 2769 (2023).

[109] T. Goldzak, X. Wang, H.-Z. Ye, and T. C. Berkelbach, Accurate thermochemistry of covalent and ionic solids from spin-component-scaled MP2, *The Journal of Chemical Physics* **157**, 174112 (2022).

[110] L. MacEnulty and D. D. O'Regan, Optimization strate- gies developed on NiO for Heisenberg exchange coupling calculations using projector augmented wave based first-principles DFT+U+J, *Phys. Rev. B* **108**, 245137 (2023).

[111] T. N. Casselman and F. Keffer, Right-Angled Superex- change, *Phys. Rev. Lett.* **4**, 498 (1960).

[112] I. De P. R. Moreira, F. Illas, and R. L. Martin, Effect of Fock exchange on the electronic structure and magnetic coupling in NiO, *Phys. Rev. B* **65**, 155102 (2002).

[113] D. Kan, A. Yamanaka, T. Terashima, and M. Takano, Preparation and optical properties of single-crystalline CaCuO₂ thin films with infinite layer structure, *Physica C: Superconductivity* **412–414**, 298 (2004).

[114] Y. Y. Peng, G. Dellea, M. Minola, M. Conn, A. Amorese, D. Di Castro, G. M. De Luca, K. Kum- mer, M. Salluzzo, X. Sun, X. J. Zhou, G. Balestrino, M. Le Tacon, B. Keimer, L. Braicovich, N. B. Brookes, and G. Ghiringhelli, Influence of apical oxygen on the extent of in-plane exchange interaction in cuprate superconductors, *Nature Phys* **13**, 1201 (2017).